Numerical Investigation of Heat Transfer in Parallel Rectangular Microchannel Heat Exchanger

MSc. Hayder Mohammed Hasan

Shatra Technical Institute, Machines and Equipments department

ABSTRACT

The axial heat conduction in parallel flow microchannel heat exchanger with rectangular ducts was numerically investigated, for laminar, 3-D, incompressible, and steady state flow of water. The governing equations, continuity, Navier-Stokes equations (momentum equations), and the energy equations for the hot and cold fluids were solved by using SIMPLE algorithm with finite volume method and FORTRAN code to obtain the temperature distribution for the two fluids and the separating wall between them.

The results play an important role of the axial heat conduction on the effectiveness in parallel flow microchannel heat exchanger and the factors affecting the axial heat conduction are; Reynolds number Re, thermal conductivity ratio K_r, aspect ratio α and channel volume. Increasing of Re, K_r, α and channel volume each separately leads to increase the axial heat conduction and vice versa.

دراسة عددية لإنتقال الحرارة في مبادل حراري مايكروي متوازي ذي قنوات مستطيلة الشكل

م.م حيدر محمد حسن

المعهد التقني في الشطرة/ قسم المكائن والمعدات

الخلاصة

عدديا تمت دراســة تأثير التوصــيل الحراري المحوري في مبادل حراري مايكروي ذي قنوات مســتطيلة الشكل لجريان متوازي طباقي ثلاثي الأبعاد للماء وفي حالة الاستقرار ولا انضـغاطي. تم حل المعادلات الحاكمة للجريان وهي معادلة الاستمرارية (continuity equation) ومعادلات الزخم (momentum equations) و معادلة الطاقة (energy equations) باســتخدام طريقة (SIMPLE method) وقد تم تحويل المعادلات

الحاكمة إلى الشـكل العددي باسـتخدام طريقة الحجوم المحددة (finite-volume method) وباسـتخدام لغة فورتران (FORTRAN). بهذه الطريقة تم إيجاد التوزيع لدرجتي حرارة المائعين والجدار الذي يفصل بينهما.

من خلال ملاحظة النتائج المسـتحصـلة من الحل العددي، تبين بأن هنالك تأثير مهم للتوصـيل الحراري المحوري على الفعالية في المبادل المايكروي كما إن هنالك مجموعة من العوامل التي تؤثر عليه وهي، عدد رينولدز(Reynolds number Re) ونسبة الموصلية الحرارية (K_r thermal conductivity ratio) والنسبة الباعية (α aspect ratio) وحجم القنوات. عند زيادة Re و K_r و α وحجم القنوات كل على حدة يزداد التوصيل الحراري المحوري، والعكس صحيح.

KEYWORDS: microchannel, heat exchanger, parallel flow, numerical solution, axial heat conduction and effectiveness.

NOMENCLACHRE

English symbols

c	specific heat . .. . J/(kgK)
C_c	heat capacity of cold fluid … *W/K*
C_h	heat capacity of hot fluid … *W/K*
C_{min}	minimum heat capacity ….. *W/K*
C_p	specific heat at constant pressure ..... J/(kgK)
D_h	hydraulic diameter . .. . *m*
H	channel height . . . . *m*
$H_{H.E}$	exchanger height .... *m*
k	thermal conductivity . . . . .*W/mK*
L	channel length . .. . *m*
$\dot{m}$	mass flow rate . . . . *kg/s*
p	pressure . . .. *Pa*
q	heat transfer rate . . ..*W*
T	temperature . . . . . *K*
t_s	separating wall thickness . . . . . *m*
u	fluid *x*-component velocity . . *m/s*
v	fluid *y*-component velocity . . . *m/s*
w	fluid *z*-component velocity ... . .*m/s*
W_{ch}	channel width . . . .*m*
$W_{H.E}$	exchanger width .... *m*
x	axial coordinate . .. .*m*

Greek symbols

ε	heat exchanger effectiveness
μ	dynamic viscosity . . . . *Pa.s*
ρ	density . . . . . *kg/m³*

Dimensionless groups

$K_r = k_s / k_f$	thermal conductivity ratio
$Re = \rho u_{h,in} D_h / \mu$	Reynolds number
$Pr = \frac{\mu C_p}{k_f}$	prandtl number
Pe=RePr	Peclet number
$\alpha = H/W$	aspect ratio

Subscripts

c	cold fluid
h	hot fluid
f	fluid
in	inlet
max	maximum value
min	minimum value
out	outlet
s	solid
u	unit
w	water

Superscripts

y horizontal coordinate . .. . m

z vertical coordinate . . . .m

1. INTRODUCTION

The fluid flow in microchannels becomes an attractive area of research during the last few years. This is due to the new applications of the microchannel flow in micro pumps, micro turbines, micro heat exchangers and other micro components. Advantages of compact structure and high heat transfer performance make the microscale heat exchangers showing a nice foreground on microelectronics, micro devices fabrication, bioengineering, micro electromechanical system (MEMS), and so on. Thus, is becoming more popular, both for commercial purposes and in scientific research [1]. Microchannel heat exchangers can be broadly classified as fluidic devices that employ channels of hydraulic diameter smaller than 1 mm [2]. Knudsen number is a measure of the degree of the rarefaction which is defined as the ratio of mean free path to the characteristic length scale of the system $Kn = \lambda / L_c$ where, λ is the mean free path and L_c is the characteristic length such as channel equivalent diameter. The flow regimes could be classified as: continuum regime when (Kn<0.001), slip flow regime (0.001<Kn<0.1), transient regime (0.1<Kn<10) and free molecular regime (Kn>10). In order to simulate the no slip flow regime, the Knudsen number is Kn<0.001. In conventional heat exchanger the solid thickness is small comparatively with the hydraulic diameter; therefore the axial heat conduction may be neglected. This means that the performance of the heat exchanger is primarily depending upon the flow in the ducts (fluid properties and mass flow rate). For microchannel heat exchanger, the solid thickness is large comparatively with the hydraulic diameter, therefore the axial heat conduction in the separating wall (solid) is important and the microchannel heat exchanger effectiveness may decrease due to the effect of axial heat conduction. The present study is deal with effect of the axial heat conduction in microchannel heat exchanger.

To understand the flow through microchannels, many researchers have been investigaty experimentally, analytically and numerically in last decade. For example, Al bakhit et al. [3] numerically investigated the flow and heat transfer in parallel flow microchannel heat exchangers. They used a hybrid approach, in which the nonlinear momentum equations for one or two channels were solved using CFD codes. The

velocity field was an input into a user developed code for solving the energy equation and they studied heat transfer for thermally developing laminar flow in two parallel rectangular channels which represent some kind of heat exchangers. From the results, it is found that in the entrance region the developing velocity profiles lead to higher values of overall heat transfer coefficient. Al-Nimr et al. [4] numerically investigated the hydrodynamics and thermal behaviors of the laminar, 2-D, fully developed, slip flow inside an insolated parallel-plate microchannel heat exchanger. They showed that both the velocity slip and the temperature jump at the walls increase with increasing Knudsen number. Yin and Bau [5] studied flow between infinite parallel plates and circular pipes to study the effect of axial heat conduction on the performance of microchannel heat exchangers. They used a fully developed velocity field and analytically they solved for temperature fields in the channel and solid wall. They found that, the axial conduction plays an important role at the entrance region. Stief et al. [6] numerically investigated the effect of solid thermal conductivity in micro heat exchangers. They showed that the reduction of conductivity of the wall material can improve the heat transfer efficiency of the exchanger due to influence of axial heat conduction in the separation wall. Also, they concluded that increasing heat capacity ratio leads to a reduction in effectiveness for all Knudsen number. Al-bakhit and Fakheri [7] numerically investigated the laminar, parallel flow microchannel heat exchanger with rectangular ducts for developing and fully developing velocity profiles with thermally developing flow in both cases. They showed that the overall heat transfer coefficient is rapidly changed for $x/D_h Pe$ (Graetz number) below 0.03, and therefore the assumption of constant overall heat transfer coefficient is not valid if the Graetz number based on the heat exchanger length is of the order of 0.03. Also, the accurate results can be obtained by solving thermally developing energy equation using fully developed velocity profiles. Mushtaq I. Hasan [8] made numerical investigation to study the counter flow microchannel heat exchanger with different channel geometries and working fluids. He studied the effect of axial heat conduction on the performance of counter flow microchannel heat exchanger with square shaped channel and he found that the existing of axial heat conduction lead to reduce the heat exchanger effectiveness.

ANALYSI

Schematic structure of a parallel flow microchannel heat exchanger with square channels is shown in figures 1 and 2 illustrated in with of channels details with rectangular profiles.

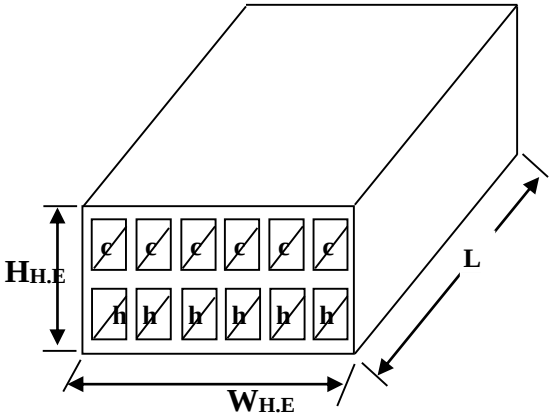

Figure 1 Schematic model of microchannel heat exchanger under concentration.

To study the entire parallel flow microchannel heat exchanger numerically, it is complicated and needs huge CPU time. Due to the symmetry between channels, the individual heat exchange unit is considered consists of two channels (hot and cold) with separating wall as shown in figure 2. Heat is transferred from hot fluid to cold fluid through the thick wall separating between them and this heat exchange unit represents a complete exchanger and gives an adequate indication about its performance.

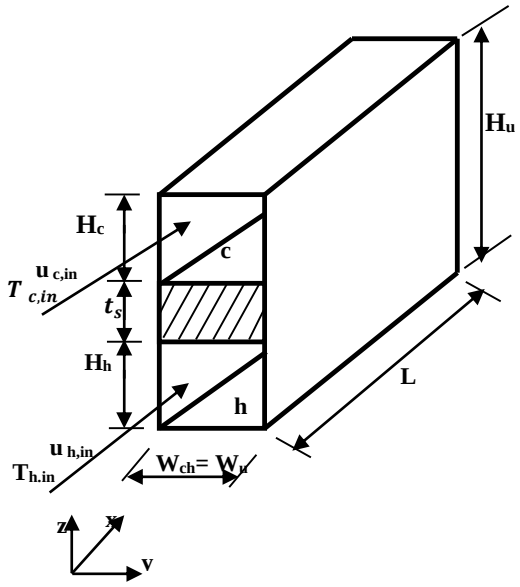

Figure 2 Three-dimensional sketch of the parallel flow heat exchanger unit.

However, the governing equations for the present model are based on the following physical and geometrical assumptions [9]:

- The flow is laminar and steady.
- The Knudsen number is small enough, so that the fluid is regard as continuous medium (no slip).
- The fluids are incompressible, Newtonian, with constant properties; in this case the water is used as working fluid.
- There is no heat transfer to/from the ambient medium.
- The energy dissipation is negligible.
- The pressure gradient is in axial direction only.
- Three dimensional of the flow and heat transfer.

The governing equations and its boundary conditions in Cartesian coordinates and nondimesionalized using the following variables according to [3]

$$x^* = \frac{x}{D_h},\ y^* = \frac{y}{D_h},\ z^* = \frac{z}{D_h},\ t_s^* = \frac{t_s}{D_h},\ W_{ch}^* = \frac{W_{ch}}{D_h}, H_i^* = \frac{H_i}{D_h},\ u_i^* = \frac{u_i}{u_{h,in}},\ v_i^* = \frac{v_i}{u_{h,in}}$$

$$, w_i^* = \frac{w_i}{u_{h,in}},\ p_i^* = \frac{p_i}{\rho u_{h,in}^2}, T_i^* = \frac{T_i - T_{c,in}}{T_{h,in} - T_{c,in}} \text{ and } \quad T_s^* = \frac{T_s - T_{c,in}}{T_{h,in} - T_{c,in}}$$

Continuity equation

$$\frac{\partial u_i^*}{\partial x^*} + \frac{\partial v_i^*}{\partial y^*} + \frac{\partial w_i^*}{\partial z^*} = 0 \qquad (1)$$

x-momentum equation

$$u_i^* \frac{\partial u_i^*}{\partial x^*} + v_i^* \frac{\partial u_i^*}{\partial y^*} + w_i^* \frac{\partial u_i^*}{\partial z^*} = -\frac{dp_i^*}{dx^*} + \frac{1}{Re_i}\left(\frac{\partial^2 u_i^*}{\partial x^{*2}} + \frac{\partial^2 u_i^*}{\partial y^{*2}} + \frac{\partial^2 u_i^*}{\partial z^{*2}}\right) \qquad (2)$$

y-momentum equation

$$u_i^* \frac{\partial v_i^*}{\partial x^*} + v_i^* \frac{\partial v_i^*}{\partial y^*} + w_i^* \frac{\partial v_i^*}{\partial z^*} = \frac{1}{Re_i}\left(\frac{\partial^2 v_i^*}{\partial x^{*2}} + \frac{\partial^2 v_i^*}{\partial y^{*2}} + \frac{\partial^2 v_i^*}{\partial z^{*2}}\right) \qquad (3)$$

z- momentum equation

$$u_i^* \frac{\partial w_i^*}{\partial x^*} + v_i^* \frac{\partial w_i^*}{\partial y^*} + w_i^* \frac{\partial w_i^*}{\partial z^*} = \frac{1}{Re_i}\left(\frac{\partial^2 w_i^*}{\partial x^{*2}} + \frac{\partial^2 w_i^*}{\partial y^{*2}} + \frac{\partial^2 w_i^*}{\partial z^{*2}}\right) \qquad (4)$$

energy equation for fluid

$$u_i^* \frac{\partial T_i^*}{\partial x^*} + v_i^* \frac{\partial T_i^*}{\partial y^*} + w_i^* \frac{\partial T_i^*}{\partial z^*} = \frac{1}{Pe_i}\left(\frac{\partial^2 T_i^*}{\partial x^{*2}} + \frac{\partial^2 T_i^*}{\partial y^{*2}} + \frac{\partial^2 T_i^*}{\partial z^{*2}}\right) \qquad (5)$$

where *i* is represented the subscript h or c which refer to the lower and upper (hot and cold) channels respectively. The diffusion equation for solid becomes

$$\frac{\partial^2 T_s^*}{\partial x^{*2}} + \frac{\partial^2 T_s^*}{\partial y^{*2}} + \frac{\partial^2 T_s^*}{\partial z^{*2}} = 0 \quad (6)$$

The dimensionless boundary conditions are:

For lower channels (hot fluid) $(0 \le z^* \le H_h^*)$

At $x^* = 0$, $0 \le y^* \le W_{ch}^*$

$$u_{h,in}^* = 1, v^* = 0, w^* = 0, T_h^* = 1$$

$$p_{h,in}^* = \frac{p_{h,in}}{\rho\, u_{h,in}^2}$$

At $x^* = \frac{L}{D_h}$, $0 \le y^* \le W_{ch}^*$

$$\frac{\partial u^*}{\partial x^*} = \frac{\partial v^*}{\partial x^*} = \frac{\partial w^*}{\partial x^*} = \frac{\partial T_h^*}{\partial x^*} = 0$$

At $y^* = 0$, $0 \le x^* \le L^*$

$$u^* = v^* = w^* = \frac{\partial T_h^*}{\partial y^*} = 0$$

At $y^* = W_{ch}^*$, $0 \le x^* \le L^*$

$$u^* = v^* = w^* = \frac{\partial T_h^*}{\partial y^*} = 0$$

At $z^* = 0$, $0 \le x^* \le L^*$, $0 \le y^* \le W_{ch}^*$

$$u^* = v^* = w^* = \frac{\partial T_h^*}{\partial z^*} = 0$$

Fluid -solid interface

At $z^* = H_h^*$, $0 \le x^* \le L^*$, $0 \le y^* \le W_{ch}^*$

$$u^* = v^* = w^* = 0$$

$$\frac{\partial T_h^*}{\partial z^*} = K_r \frac{\partial T_s^*}{\partial z^*}$$

For upper channel (cold fluid) $(H_h^* + t_s^* \le z^* \le H_u^*)$

At $x^* = 0$, $0 \le y^* \le W_{ch}^*$

$$u_{c,in}^* = \frac{u_{c,in}}{u_{h,in}}, v^* = w^* = T_c^* = 0$$

$$p_{c,in}^* = \frac{p_{c,in}}{\rho\, u_{h,in}^2}$$

At $x^* = \frac{L}{D_h}$, $0 \le y^* \le W_{ch}^*$

$$\frac{\partial u^*}{\partial x^*} = \frac{\partial v^*}{\partial x^*} = \frac{\partial w^*}{\partial x^*} = \frac{\partial T_c^*}{\partial x^*} = 0$$

At $y^* = 0$, $0 \le x^* \le L^*$

$$u^* = v^* = w^* = \frac{\partial T_c^*}{\partial y^*} = 0$$

At $y^* = W_{ch}^*$, $0 \le x^* \le L^*$

$$u^* = v^* = w^* = \frac{\partial T_c^*}{\partial y^*} = 0$$

At $z^* = H_u^*$,$0 \le x^* \le L^*$, $0 \le y^* \le W_{ch}^*$

$$u^* = v^* = w^* = \frac{\partial T_c^*}{\partial z^*} = 0$$

Fluid -solid interface

At $z^* = H_h^* + t_s^*$,$0 \le x^* \le L^*$, $0 \le y^* \le W_{ch}^*$

$$u^* = v^* = w^* = 0$$

$$\frac{\partial T_c^*}{\partial z^*} = K_r \frac{\partial T_s^*}{\partial z^*}$$

Solid wall boundary conditions ($H_h^* \le z^* \le H_h^* + t_s^*$)

At $x^* = 0$,$0 \le y^* \le W_{ch}^*$

$$\frac{\partial T_s^*}{\partial x^*} = 0$$

At $x^* = \frac{L}{D_h}$, $0 \le y^* \le W_{ch}^*$

$$\frac{\partial T_s^*}{\partial x^*} = 0$$

At $y^* = 0$, $0 \le x^* \le L^*$

$$\frac{\partial T_s^*}{\partial y^*} = 0$$

At $y^* = W_{ch}^*$, $0 \le x^* \le L^*$

$$\frac{\partial T_s^*}{\partial y^*} = 0$$

At $z^* = H_h^*$, $0 \le x^* \le L^*$, $0 \le y^* \le W_{ch}^*$

$$\frac{\partial T_h^*}{\partial z^*} = K_r \frac{\partial T_s^*}{\partial z^*}$$

At $z^* = H_h^* + t_s^*, 0 \le x^* \le L^*$, $0 \le y^* \le W_{ch}^*$

$$\frac{\partial T_c^*}{\partial z^*} = K_r \frac{\partial T_s^*}{\partial z^*}$$

By solving the above governing equations using FORTRAN code the temperature distribution is determined in the hot, cold fluid and solid domains. From these distributions one can determine the axial heat conduction and exchanger effectiveness.

Heat exchanger effectiveness is the ratio of actual heat transfer to the maximum possible heat that can be transferred [10]:

$$\varepsilon = \frac{q}{q_{max.possible}} \quad (7)$$

where

$$q_{max} = C_{min}(T_{h,in} - T_{c,in}) \quad (8)$$

and

$$q = C_c (T_{c,out} - T_{c,in}) = C_h (T_{h,in} - T_{h,out}) \quad (9)$$

where $C_h = m_h c_h$ and $C_c = m_c c_c$

then the effectiveness is

$$\varepsilon = \frac{C_c(T_{c,out} - T_{c,in})}{C_{min}(T_{h,in} - T_{c,in})} = \frac{C_h(T_{h,in} - T_{h,out})}{C_{min}(T_{h,in} - T_{c,in})} \quad (10)$$

For the axial heat conduction in section *x* is

$$q''_x = \left(k_s \frac{\bar{T}_{s,i} - \bar{T}_{s,i+1}}{\Delta x} \right)_x \quad (11)$$

where, $\bar{T}_{s,i}$ is the average solid temperature, $\bar{T}_{s,i+1}$ at the next section and Δ the distance between the two sections as shown in figure 3.

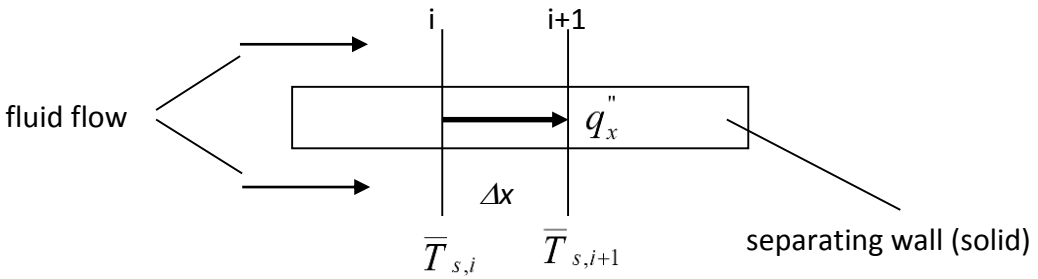

Figure 3 Schematic of separating wall.

2. NUMERICAL SOLUTION

Finite-volume method adopted which is applied to the integral form of the governing equations over the control volume (cell) as shown in figure 4. A cell containing node ***P*** has four neighbouring nodes identified as west, east, south and north nodes ***(W, E, S, N).*** The notation, ***w, e, s and n*** are used to refer to the west, east, south and north cell faces respectively. The methods which depend on this technique such central differencing scheme, upwind differencing scheme, hybrid differencing scheme and others. However, the present work is adopted on the hybrid differencing scheme with staggered grids arrangement to solve pressure-velocity coupling which associated with present problem and SIMPLE algorithm is used as listed in [11].

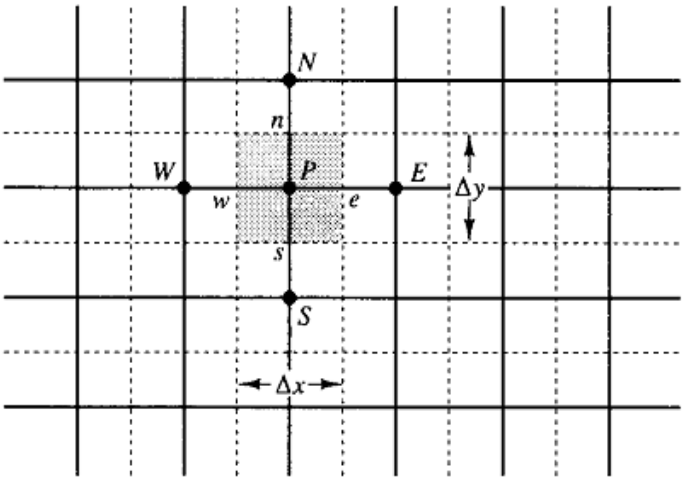

Figure 4 A cells in two-dimensional and neighbouring nods taken from [11].

SIMPLE algorithm is implicit method are preferred for steady state and slow transient flows, because they have less stringent time steps restrictions as compared the explicit schemes. Many solutions methods for steady incompressible flows use a pressure (or pressure-correction) equation to solve pressure-velocity coupling [12]. Discretized *u*-component equation (2) is written in the following form [11]

$$a^*_{(i,J,K)}u^*_{i(i,J,K)} = \sum a^*_{nb}u^*_{i(nb)} + \left(p^*_{i(I-1)} - p^*_{i(I)}\right)A^*_x \qquad (12)$$

where, $\sum a^*_{nb} u^*_{i(nb)}$ is the summation of neighboring components for *u*-component and the subscript *i* refer to cold or hot fluid. The values of coefficients $a^*_{(i,J,K)}$ and a^*_{nb} in equation (12) are calculated by using the hybrid method. However, to initiate the SIMPLE calculation process a pressure field $p^{*\cdot}_i$ is guessed. Discretised momentum equation (2) is solved using the guessed pressure field to yield velocity component $u^{*\cdot}_i$ as follows [11]

$$a^*_{(i,J,K)} u^{*\cdot}_{i(i,J,K)} = \sum a^*_{nb} u^{*\cdot}_{i(nb)} + \left(p^{*\cdot}_{i(I-1)} - p^{*\cdot}_{i(I)}\right) A^*_x \tag{13}$$

Now we defined the correction $p^{*''}_i$ as the difference between the correct pressure field p^*_i and the guessed pressure field $p^{*\cdot}_i$, so that

$$p^*_i = p^{*\cdot}_i + p^{*''}_i \tag{14}$$

Similarly we defined velocity correction $u^{*''}_i$ to relate the correct velocity u^*_i to the guessed velocity solution $u^{*\cdot}_i$

$$u^*_i = u^{*\cdot}_i + u^{*''}_i \tag{15}$$

Subtraction of equation (13) from equation (12) gives

$$a^*_{(i,J,K)}\left(u^*_{i(i,J,K)} - u^{*\cdot}_{i(i,J,K)}\right) = \sum a^*_{nb}\left(u^*_{i(nb)} - u^{*\cdot}_{i(nb)}\right) + \left[\left(p^*_{i(I-1)} - p^{*\cdot}_{i(I-1)}\right) - \left(p^*_{i(I)} - p^{*\cdot}_{i(I)}\right)\right] A^*_x \tag{16}$$

Using correction formulae (14) and (15), the equation (16) may be rewritten as follows

$$a^*_{(i,J,K)} u^{*''}_{i(i,J,K)} = \sum a^*_{nb} u^{*''}_{i(nb)} + \left(p^{*''}_{i(I-1)} - p^{*''}_{i(I)}\right) A^*_x \tag{17}$$

At this point an approximation is introduced: $\sum a^*_{nb} u^*_{i(nb)}$ is dropped to simplify equation (17) for velocity correction. Omission of that term is the main approximation of the SIMPLE [11]. We obtain

$$u^{*''}_{i(i,J,K)} = d^*_{(i,J,K)}\left(p^{*''}_{i(I-1)} - p^{*''}_{i(I)}\right) \tag{18}$$

where $d^*_{(i,J,K)} = A^*_x / a^*_{(i,J,K)}$. Equation (18) describe the correction to be applied to *u*-component through equation (15), which gives

$$u^*_{i(i,J,K)} = u^{*\cdot}_{i(i,J,K)} + d^*_{(i,J,K)}\left(p^{*''}_{i(I-1)} - p^{*''}_{i(I)}\right) \tag{19}$$

Similar expression exist for $u^*_{i(i+1,J,K)}$ [11]

$$u^*_{i(i+1,J,K)} = u^{*\cdot}_{i(i+1,J,K)} + d^*_{(i+1,J,K)}\left(p^{*''}_{i(I)} - p^{*''}_{i(I+1)}\right) \tag{20}$$

where $d^{*}_{(i+1,J,K)} = A^{*}_{x} \Big/ a^{*}_{(i+1,J,K)}$.

The SIMPLE algorithm gives a method of calculating pressure and velocity. The method is iterative and when other scalars like present problem are coupled to the momentum equations, the calculations needs to be done sequentially [11]. The sequence

of operations in a FORTRAN procedure which employs the SIMPLE algorithm is given in figure 5.

In figure 5, the correct pressure field p_i^{*} and correct velocity field u_i^{*}, v_i^{*} and w_i^{*} for two channels are obtained separately. There is no coupling between the two channels for these variables as shown in the steps 1, 2 and 3. The previous steps represent the solution for pressure-velocity coupling problem (pressure-correction method). While, the last step represent the solution for convection-conduction conjugate heat transfer problem (simultaneously solution for the temperatures), where

$$b^{*}_{(I,J,K)} = \left(u^{*\bullet}_{(i,J,K)} - u^{*\bullet}_{(i+1,J,K)}\right)A^{*}_{x} + \left(v^{*}_{(I,j,K)} - v^{*}_{(I,j+1,K)}\right)A^{*}_{y} + \left(w^{*}_{(I,J,k)} - w^{*}_{(I,J,k+1)}\right)A^{*}_{z} \quad (21)$$

the A^{*}_{x}, A^{*}_{y} *and* A^{*}_{z} represents the control volume face area in *x*, *y* and *z* directions.

The pressure field p_i^{*} is obtained by solving the pressure correction $p_i^{*"}$ equation. It is common practice to fix the absolute pressure at one inlet node and set the pressure correction to zero ($p_i^{*"}$ =0) at that node. Having specified a reference value, the absolute pressure field inside the domain can now be obtained [11].

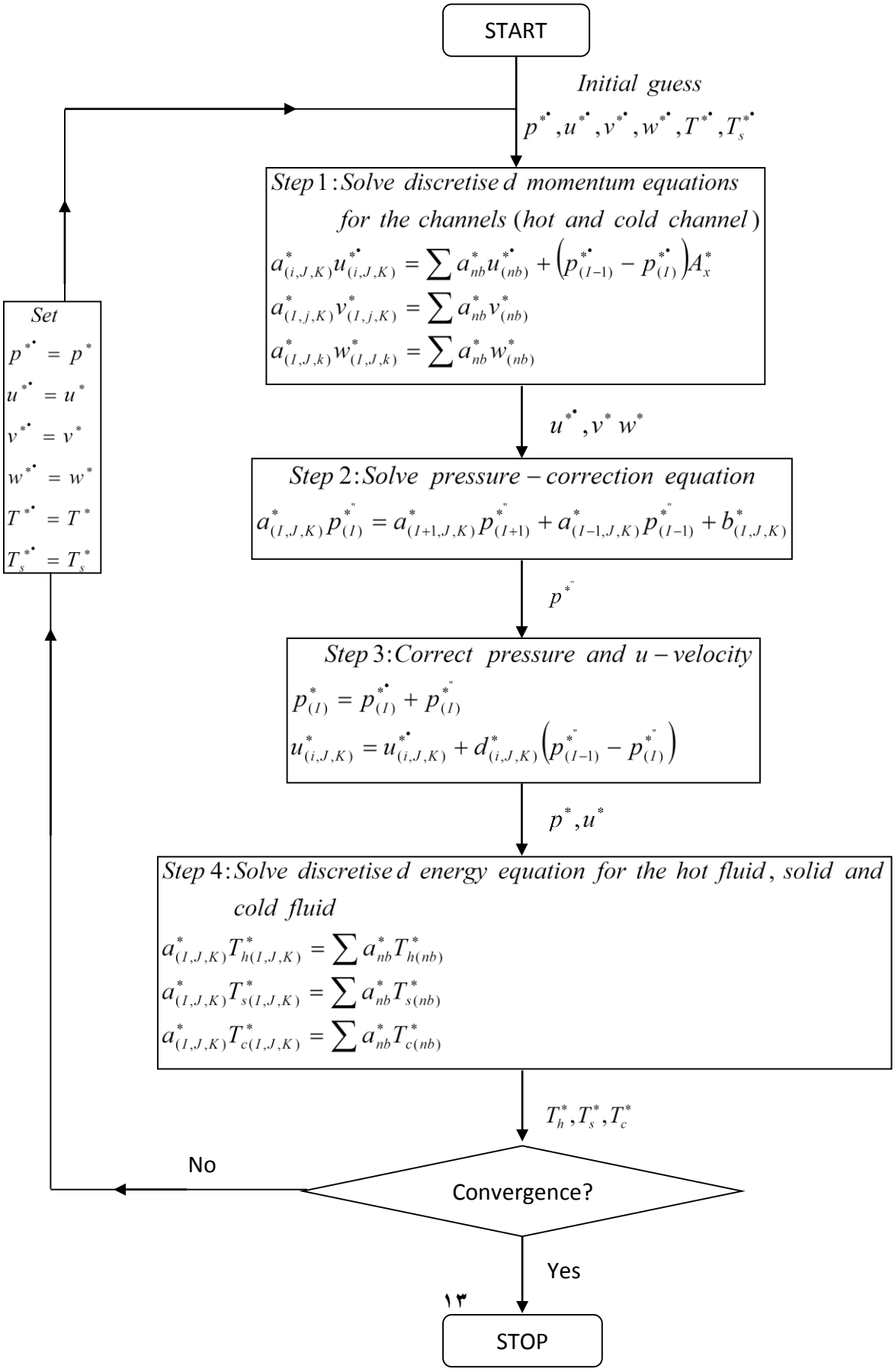
START
Initial guess
$p^{*\bullet}, u^{*\bullet}, v^{*\bullet}, w^{*\bullet}, T^{*\bullet}, T_s^{*\bullet}$
Step 1: Solve discretised momentum equations for the channels (hot and cold channel)
$a^*_{(i,J,K)} u^{*\bullet}_{(i,J,K)} = \sum a^*_{nb} u^{*\bullet}_{(nb)} + \left(p^{*\bullet}_{(I-1)} - p^{*\bullet}_{(I)}\right) A^*_x$
$a^*_{(I,j,K)} v^*_{(I,j,K)} = \sum a^*_{nb} v^*_{(nb)}$
$a^*_{(I,J,k)} w^*_{(I,J,k)} = \sum a^*_{nb} w^*_{(nb)}$
$u^{*\bullet}, v^* w^*$
Step 2: Solve pressure – correction equation
$a^*_{(I,J,K)} p^{*"}_{(I)} = a^*_{(I+1,J,K)} p^{*"}_{(I+1)} + a^*_{(I-1,J,K)} p^{*"}_{(I-1)} + b^*_{(I,J,K)}$
$p^{*"}$
Step 3: Correct pressure and u – velocity
$p^*_{(I)} = p^{*\bullet}_{(I)} + p^{*"}_{(I)}$
$u^*_{(i,J,K)} = u^{*\bullet}_{(i,J,K)} + d^*_{(i,J,K)} \left(p^{*"}_{(I-1)} - p^{*"}_{(I)}\right)$
p^*, u^*
Step 4: Solve discretised energy equation for the hot fluid, solid and cold fluid
$a^*_{(I,J,K)} T^*_{h(I,J,K)} = \sum a^*_{nb} T^*_{h(nb)}$
$a^*_{(I,J,K)} T^*_{s(I,J,K)} = \sum a^*_{nb} T^*_{s(nb)}$
$a^*_{(I,J,K)} T^*_{c(I,J,K)} = \sum a^*_{nb} T^*_{c(nb)}$
T^*_h, T^*_s, T^*_c
Convergence?
No
Yes
Set
$p^{*\bullet} = p^*$
$u^{*\bullet} = u^*$
$v^{*\bullet} = v^*$
$w^{*\bullet} = w^*$
$T^{*\bullet} = T^*$
$T_s^{*\bullet} = T_s^*$
STOP

Figure 5 The SIMPLE algorithm.

4. RESULTS

In this section, the results about the influences of Reynolds number Re, thermal conductivity ratio *Kr*, aspect ratio α and channel volume on the local and average axial heat conduction (q''_x and $q''_{average}$) and the effectiveness to average axial heat conduction ratio $\varepsilon / q''_{average}$ in parallel flow rectangular microchannel heat exchanger for different conditions is studied. Study the ratio $\varepsilon / q''_{average}$ to indicate the effect of axial conduction on the exchanger effectiveness, but before that it's necessary to study the $q''_{average}$ and ε each separately.

In order to verify the accuracy of present numerical model, a comparison is made between the results of present model for rectangular microchannel heat exchanger and that in literature. Figure 6 represents a comparison for dimensionless mean temperature for hot and cold fluids in rectangular microchannel heat exchanger for present numerical model and that of [7]. The dimensionless mean temperature $T_m^* = \frac{T_i - T_{c,in}}{T_{h,in} - T_{c,in}}$ is presented in this figure for the hot and cold fluids in rectangular microchannel heat exchanger against the dimensionless axial distance $x^+ = \frac{x}{D_h \, \mathrm{Re} \, \mathrm{Pr}}$ at Re=100, Pr=0.7 and $\frac{k_w D_h}{k_s t_s}$ =100. The figure indicates for both results that dimensionless mean temperature converge to each other toward fully developed region, this refer to that the heat is transferred from hot to cold fluid. Also, the figure shows that there is a good agreement between the present numerical results and the results of [7], the maximum percentage error was ±2.01%.

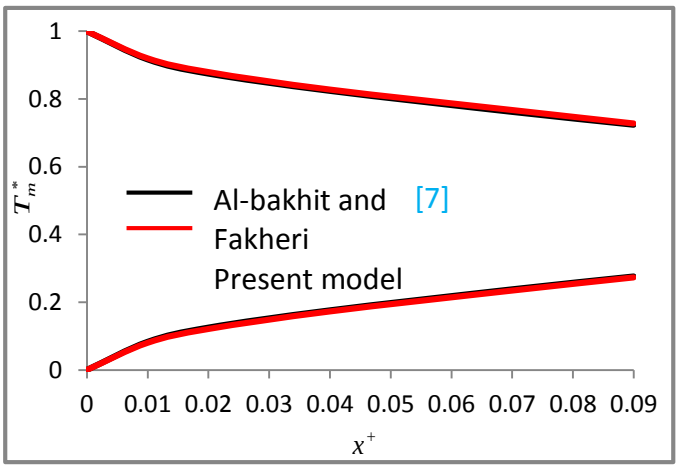

Figure 6 Comparison of the dimensionless mean temperature of the hot and cold fluids.

Figure 7 shows the longitudinal variation of the axial heat conduction $q_x^{"}$ with axial distance x for different thermal conductivity ratios K_r at t_s=50μm, Re=200 and α=1. For all thermal conductivity ratios, the figure indicates that the $q_x^{"}$ is high in entrance region and decrease toward fully developed region due to the effect of entrance. Also, the figure shows that the $q_x^{"}$ increases with K_r, due to that the heat transferred from hot fluid to cold fluid increase with increase K_r.

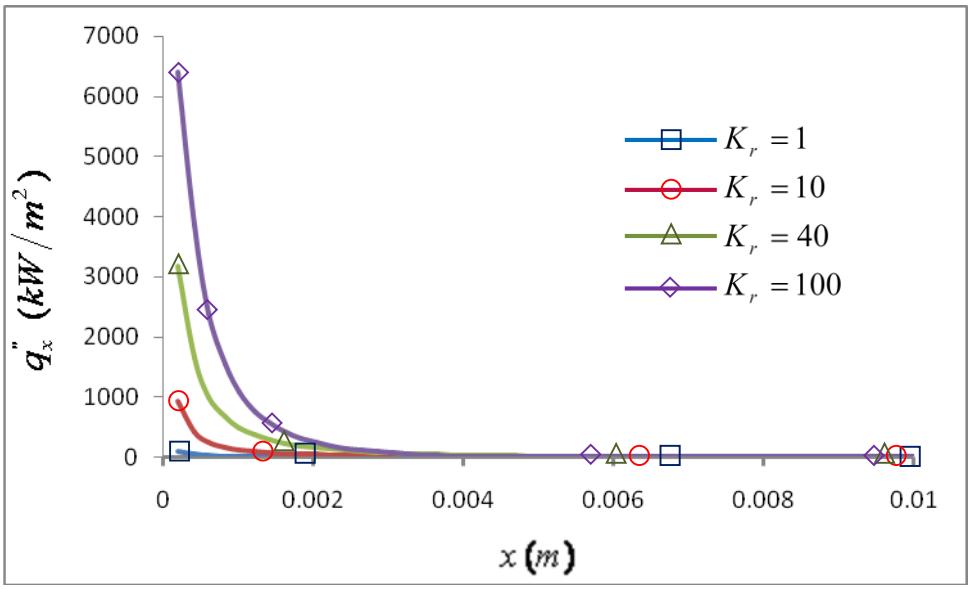

Figure 7 Longitudinal variation of the axial heat conduction with axial distance *x* for different values of K_r.

Figure 8 shows the variation of longitudinal axial heat conduction in the separating wall q''_x with axial distance *x* for different Reynolds numbers at K_r=1, t_s=50μm and α=1. This figure shows that the q''_x for all Reynolds number is high in the entrance region, due to the effect entrance region since maximum heat transfer accrued in the entrance region and as a result maximum value of axial heat conduction is also created in this region. As the heat transfer process increased with increasing Re and so, the fraction of axial conduction increased. Also, as q''_x increased with Re, the heat transferred from hot fluid to cold fluid decrease and both fluids and separating wall are still conserve heat and there is no sufficient time for heat exchange at high Re.

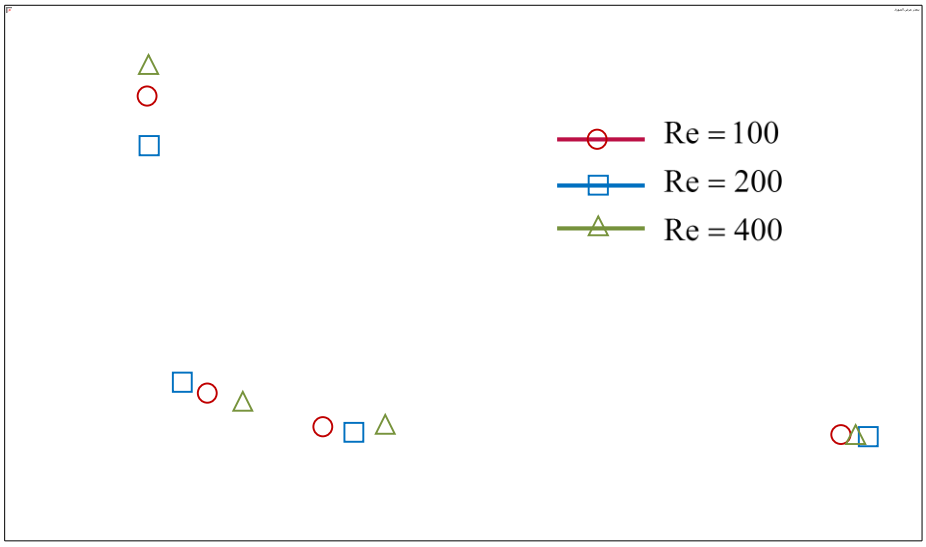

Figure 8 Longitudinal variation of the axial heat conduction with axial distance *x* for different Reynolds numbers.

Figure 9 illustrates the variation of average axial heat conduction $q''_{average}$ with Reynolds number Re for different aspect ratios at K_r=1 and t_s=50μm. For all α, the $q''_{average}$ increases with Re for the raised reason is the same in pervious figure. Also, $q''_{average}$ decrease when α decrease, this is refer to the cowing of heat transferred between both fluids overcome on the axial conduction in small α and vice versa.

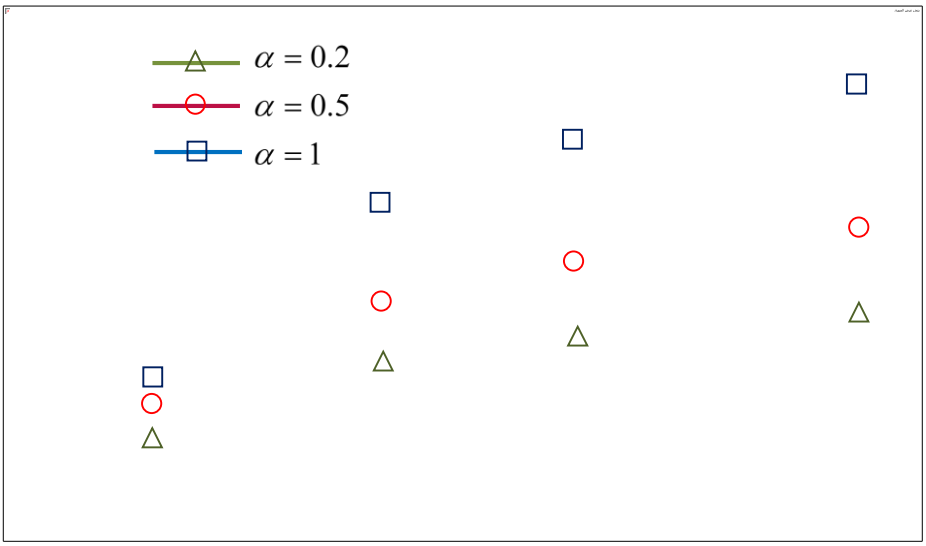

Figure 9 Variation of the average axial heat conduction with Reynolds number for different aspect ratios.

Figure 10 shows the variation of the average axial heat conduction $q''_{average}$ with aspect ratio α for different Reynolds numbers at K_r =1 and t_s =50μm. For all Re, $q''_{average}$ increases with α, this is because any increasing of fluid in the channel leads to increasing the heat remaining in the fluids and separating wall and then the $q''_{average}$ increase. As illustrated in previous figures $q''_{average}$ increase with Re.

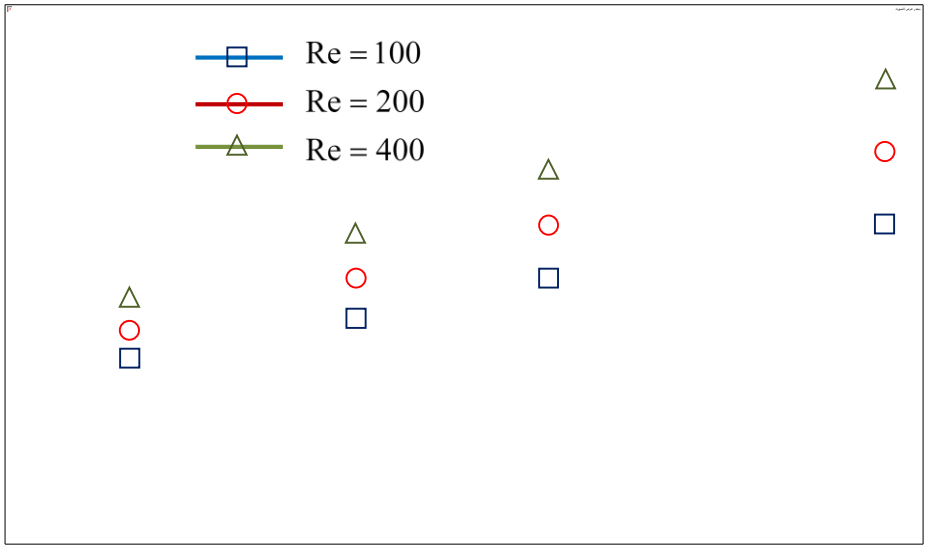

Figure 10 Variation of the average axial heat conduction with aspect ratio for different Reynolds.

Figure 11 shows the variation of the average axial heat conduction $q''_{average}$ with thermal conductivity ratio K_r for different Reynolds numbers at t_s =50μm and α=1 and. For all Re, $q''_{average}$ increases with K_r, this is because that more heat transferred between the two fluids through the separating wall at high K_r, and this lead to increase the axial heat conduction.

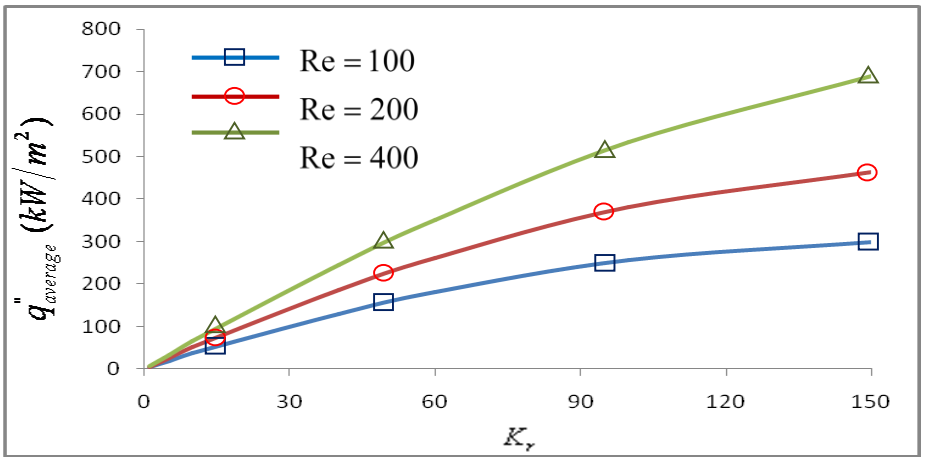

Figure 11 Variation of the average axial heat conduction with thermal conductivity ratio for different Reynolds numbers.

Figure 12 shows the variation of the average axial heat conduction $q''_{average}$ in axial direction with aspect ratio α for different thermal conductivity ratios at Re=200 and t_s =50μm. For all K_r, the $q''_{average}$ increases with α (due to increasing of fluid in the channel lead to increasing the heat remaining in the fluids and separating wall). Also, $q''_{average}$ increases with K_r because the heat transferred through the separating wall increases.

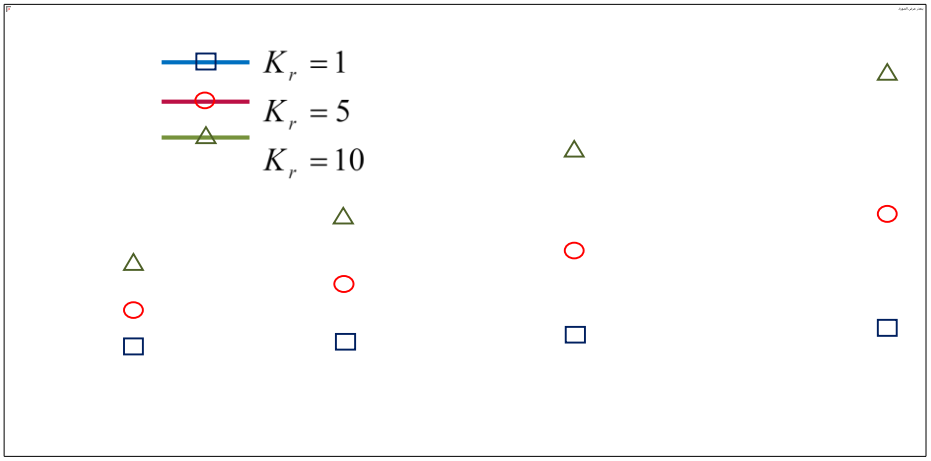

Figure 12 Variation of the average axial heat conduction with aspect ratio for different thermal conductivity ratios.

Figure 13 clarifies the variation of the average heat conduction in axial direction $q''_{average}$ with channel volume for different Reynolds number at K_r=1 and t_s=50μm. For all Re, $q''_{average}$ increases with channel volume in which lead to increasing the heat remaining in the fluid and separating wall and then the $q''_{average}$ increase.

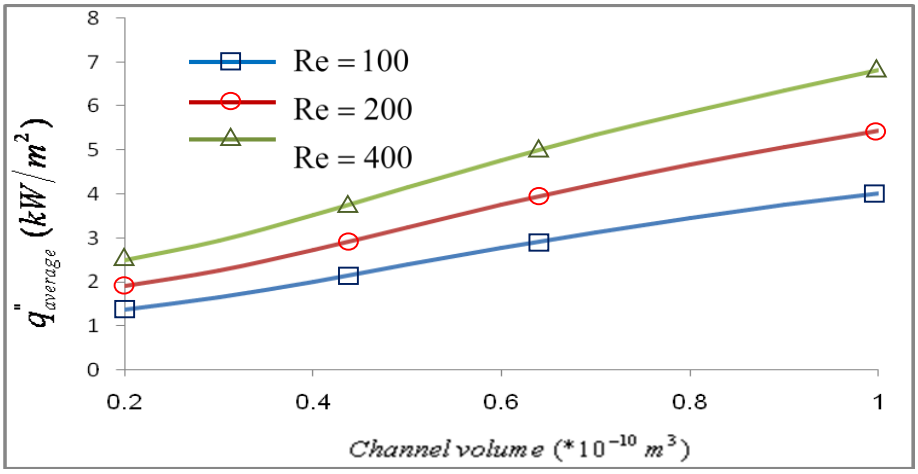

Figure 13 Variation of the average axial heat conduction with channel volume for different Reynolds numbers.

Figure 14 shows the variation of the average heat conduction in axial direction $q''_{average}$ with channel volume for different thermal conductivity ratios at Re=200 and t_s =50μm. For all K_r, $q''_{average}$ increases with channel volume. Also, $q''_{average}$ increase with K_r in which heat transferred between the two fluids through the separating wall increases.

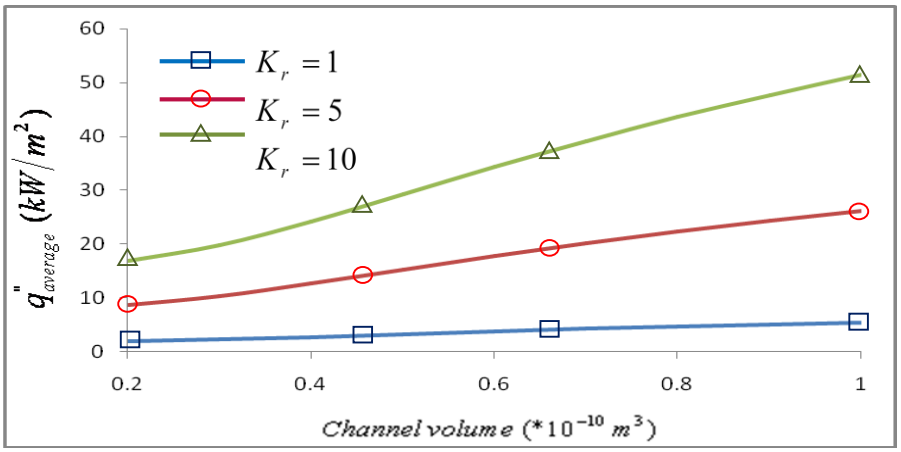

Figure 14 Variation of the average axial heat conduction with channel volume for different thermal conductivity ratios.

Figure 15 illustrates the variation of the microchannel heat exchanger effectiveness ε with Reynolds number for different aspect ratios at K_r=1 and t_s=50μm. The effectiveness decrease with Re for all α, this is due to that the amount fluid increases when Re increase and then ΔT decrease. On other hand, the axial conduction in the solid also increase with Re as before. The effectiveness at low Re is seems to be converge to each other but the difference increase at high Re, this refer to low Re (there is sufficient time to heat exchange and the effect of axial conduction is small in all cases and vice versa). On other hand, ε is increased at low α, and at α=0.2 gives best ε because the axial conduction decrease and heat transferred increase.

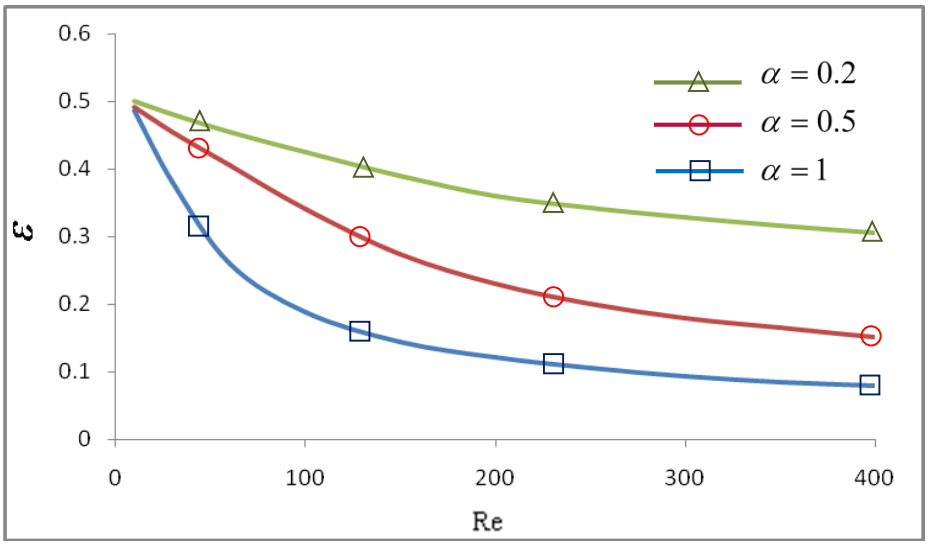

Figure 15 Variation of the microchannel heat exchanger effectiveness with Reynolds number for different aspect ratios.

Figure 16 illustrates the variation of microchannel heat exchanger effectiveness ε with thermal conductivity ratio K_r at α=1 and t_s=50μm for different Reynolds numbers. For all Re, the effectiveness increases with increase K_r and more heat transferred from hot to cold fluid in spite of the axial conduction, also increases with K_r, but the heat transfer overcome on it. Also, the figure indicates that the ε is higher at Re=100.

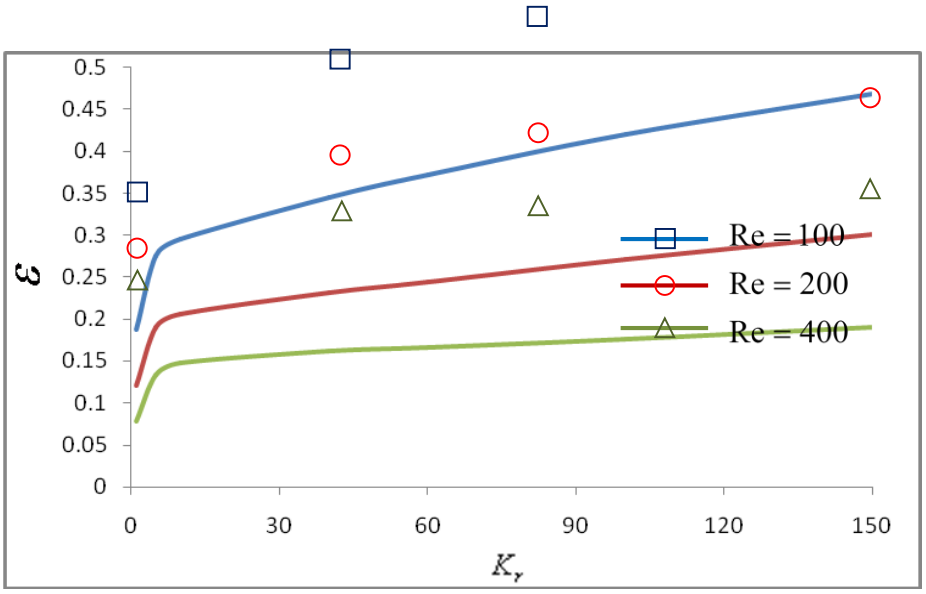

Figure 16 Variation of the heat exchanger effectiveness with thermal conductivity ratios for different Reynolds numbers.

Figure 17 shows the variation of the microchannel heat exchanger effectiveness ε with aspect ratio α for different Reynolds numbers at K_r =1 and t_s =50μm. For all Re, the figure clarifies that the effectiveness decreases with α. This is due to the amount of fluid increases when α increase and then ΔT decrease. On other hand, the axial conduction in the solid also increases with α as shown before. Also, the figure shows that, the effectiveness at Re=100 is more than the others for same reason.

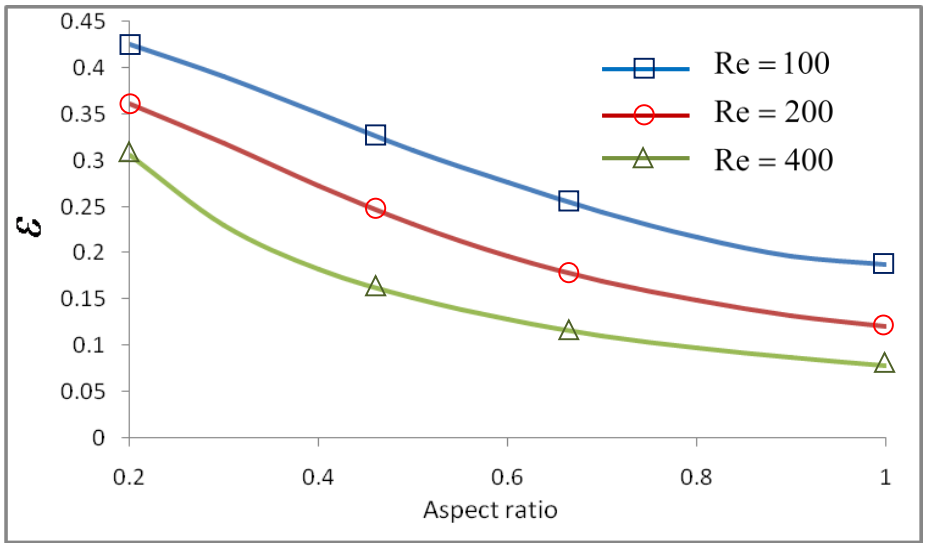

Figure 17 Variation of the heat exchanger effectiveness with aspect ratio for different Reynolds numbers.

Figure 18 illustrates the variation of the microchannel heat exchanger effectiveness ε with channel volume for different thermal conductivity ratios at Re=200 and t_s =50μm. For all K_r, the effectiveness decreases with channel volume. This is due to the amount of fluid increases when channel volume increase and then ΔT decrease.

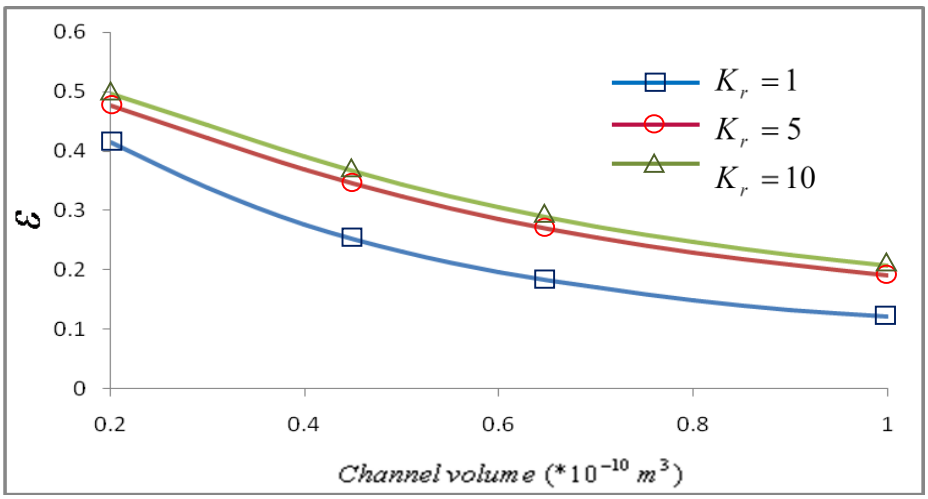

Figure 18 Variation of the heat exchanger effectiveness with channel volume for different thermal conductivity ratios.

Figure 19 shows the variation of the microchannel heat exchanger effectiveness ε with thermal conductivity ratio K_r for different aspect ratios at Re=200 and t_s =50μm. The ε increases with K_r this is due to increasing the conductivity of the separating wall and more heat is transferred in this case in spite of the axial conduction also increases, but the heat transferred between the two fluids overcome on it. Also, the ε at α=0.2 more than the others, this is because the amount of fluid decreases when the α decrease. For α=0.2 the effectiveness increase with K_r but normally not above ε=0.5 for nearly K_r =10 then the effectiveness will be constant.

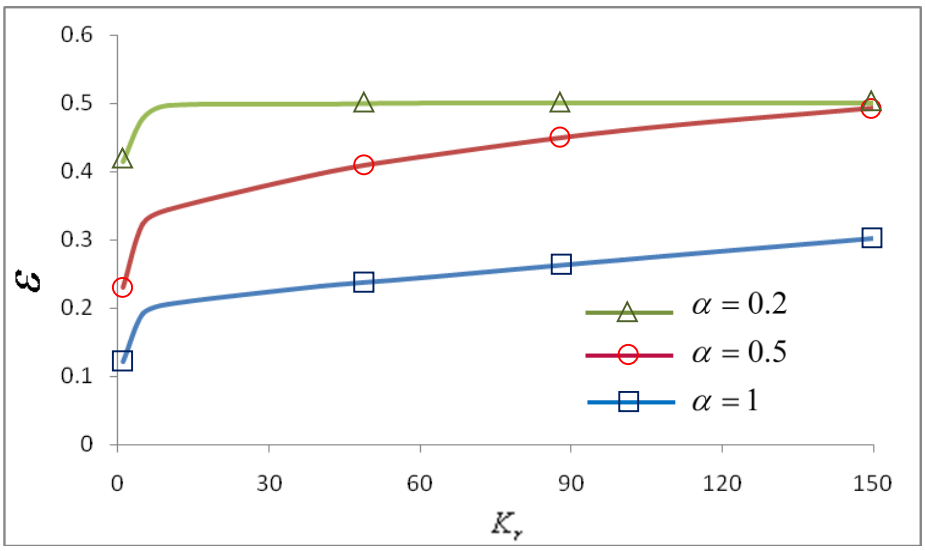

Figure 19 Variation of the heat exchanger effectiveness with thermal conductivity ratio for different aspect ratios.

Figure 20 illustrates the variation of the microchannel heat exchanger effectiveness to average axial conduction ratio $\varepsilon/q''_{average}$ with Reynolds number for different aspect ratios at K_r =1 and t_s =50μm. For all α, $\varepsilon/q''_{average}$ decreases with Re, this is because the effectiveness decreases and the axial conduction in the solid increases with Re. For α=0.2 gives the best value of $\varepsilon/q''_{average}$ especially at low Re due to both the ε increase and $q''_{average}$ decrease at small Re.

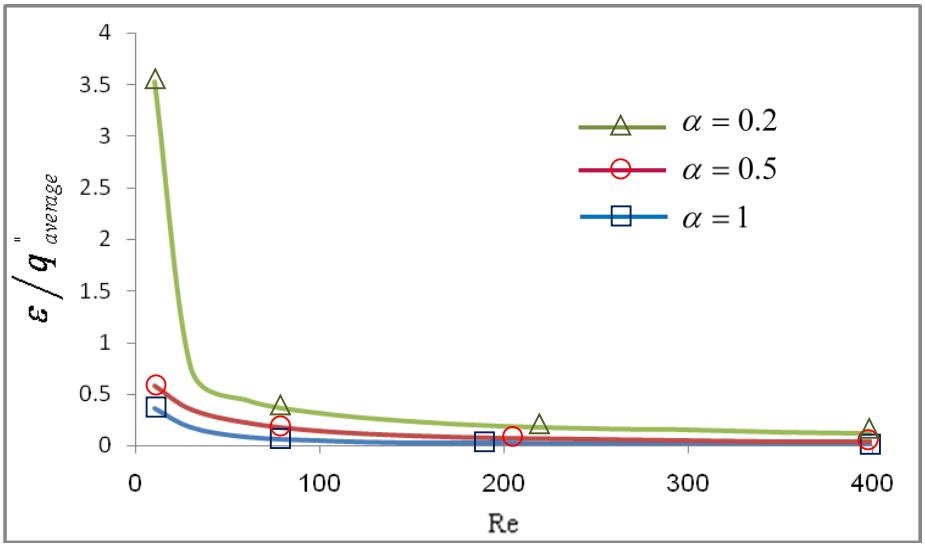

Figure 20 Variation of the microchannel heat exchanger effectiveness to average axial heat conduction ratio with Reynolds number for different aspect ratios.

Figure 21 shows the variation of the microchannel heat exchanger effectiveness to average axial heat conduction ratio $\varepsilon/q''_{average}$ with thermal conductivity ratio for different aspect ratios at Re=200 and t_s =50μm. $\varepsilon/q''_{average}$ decreases with K_r, this is due to the $q''_{average}$ increases with K_r, in spite of that ε also increase in this case, but the increasing in $q''_{average}$ is more than that for the ε. Also, at α=0.2 gives the best value of $\varepsilon/q''_{average}$.

\

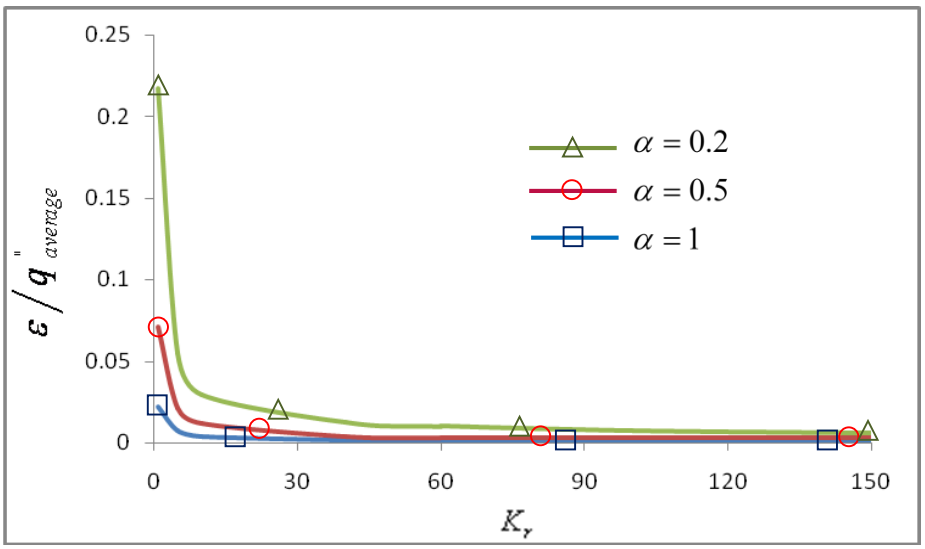

Figure 21 Variation of the microchannel heat exchanger effectiveness to average axial heat conduction ratio with thermal conductivity ratio for different aspect ratios.

Figure 22 illustrates the variation of the microchannel heat exchanger effectiveness to average axial heat conduction ratio $\varepsilon/q''_{average}$ with thermal conductivity ratio K_r for different Reynolds numbers at α=1 and t_s =50μm. For all Re, as expected $\varepsilon/q''_{average}$ is decrease with K_r. Also, $\varepsilon/q''_{average}$ decrease with Re, since amount of fluid increases when Re increase then ΔT and ε decreases. On other hand, the axial conduction in the solid also increase with Re.

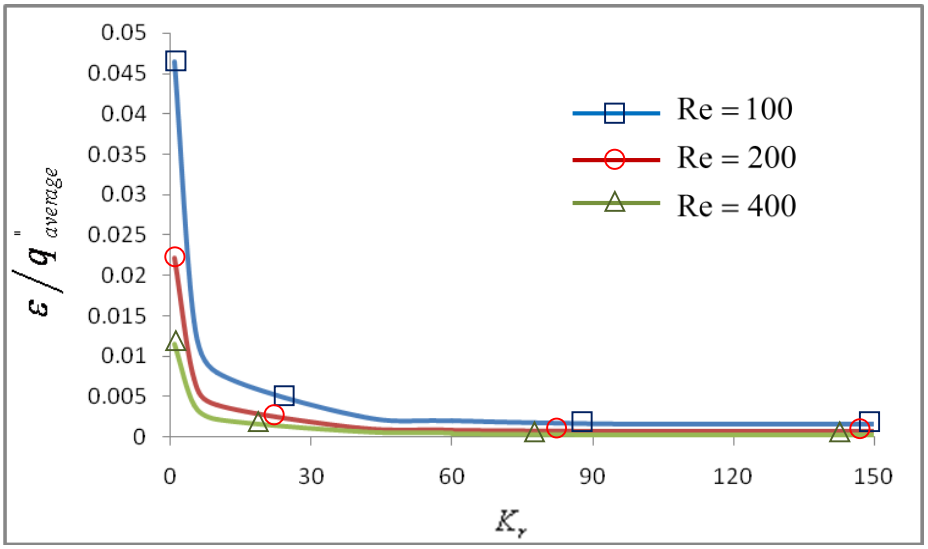

Figure 22 Variation of the microchannel heat exchanger effectiveness to average axial heat conduction ratio with thermal conductivity ratio for different Reynolds numbers.

Figure 23 shows the variation of the microchannel heat exchanger effectiveness to average axial heat conduction ratio $\varepsilon/q''_{average}$ with channel volume for different Reynolds numbers at K_r =1 and t_s =50μm. For all Re, $\varepsilon/q''_{average}$ decreases with channel volume this is due to the effectiveness decreases with channel volume and the axial conduction in the solid increases with channel volume.

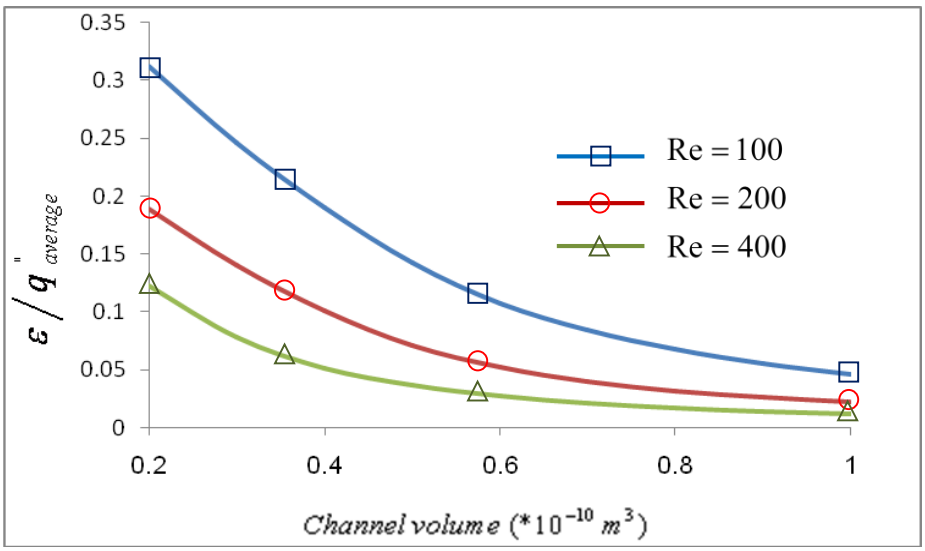

Figure 23 Variation of the microchannel heat exchanger effectiveness to average axial heat conduction ratio with channel volume for different Reynolds numbers.

Figure 24 shows the variation of the microchannel heat exchanger effectiveness to average axial heat conduction ratio $\varepsilon/q''_{average}$ with channel volume for different thermal conductivity ratios at Re=200 and t_s =50μm. It seen from this figure the best ratio of $\varepsilon/q''_{average}$ is at K_r =1.

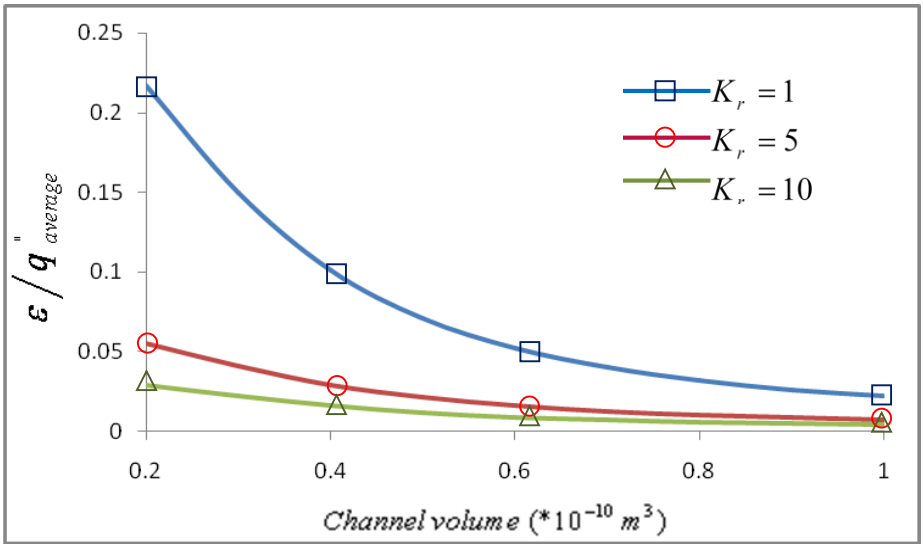

Figure 24 Variation of the microchannel heat exchanger effectiveness to average axial heat conduction ratio with channel volume for different thermal conductivity ratios.

5. CONCLUSIONS

The effects of axial heat conduction in rectangular microchannel heat exchanger with parallel flow was studied numerically through the microchannel heat exchanger effectiveness to average axial conduction ratio $\varepsilon/q''_{average}$ considering thermally and hydradynamically developing flow conditions. The Navier–Stokes and energy equations are solved in a three-dimensional domain using the finite-volume method with FORTRAN code. However, from the results obtained the following conclusions can be drawn:

- The parameters affect the axial conduction and the effectiveness in rectangular microchannel heat exchanger are: thermal conductivity ratio K_r , Reynolds number Re, aspect ratio α and channel volume.
- Increasing of the thermal conductivity ratio K_r , Reynolds number Re, aspect ratio α and channel volume each separately lead to increase of the axial heat conduction and vice versa.

- The microchannel heat exchanger effectiveness ε increase with increasing thermal conductivity ratio K_r while decrease with increasing Reynolds number Re, aspect ratio α and channel volume each separately.
- The effect of the axial heat conduction is reflected in the microchannel heat exchanger effectiveness to average axial heat conduction ratio $\varepsilon / q''_{average}$ which decrease with increasing thermal conductivity ratio K_r in spite of the effectiveness increase due to the axial heat conduction effect, and increasing of K_r will not enhance the effectiveness, and $\varepsilon / q''_{average}$ decreases with Reynolds number Re, aspect ratio α and channel volume each separately.

REFERENCES

[1] M.A. Al-Nimr, M. Maqableh, A.F. Khadrawi, S.A. Ammourah," Fully developed thermal behaviors for parallel flow microchannel heat exchanger", International Communications in Heat and Mass Transfer, Vol. 36, pp. 385-390, 2009.

[2] B. Mathew, H. Hegab, "Application of effectiveness-NTU relationship to parallel flow microchannel heat exchangers subjected to external heat transfer", International Journal of Thermal Sciences, Vol. 30, pp.1-10, 2009.

[3] H. Al-bakhit and A. Fakheri, "A hybrid Approach for Full Numerical Simulation of Heat Exchangers", ASME Heat Transfer Summer Conference, San Francisco, CA, USA, pp. 17-22, 2005.

[4]M.A. Al-Nimr, M. Maqableh, A.F. Khadrawi, S.A. Ammourah," Fully developed thermal behaviors for parallel flow microchannel heat exchanger", International Communications in Heat and Mass Transfer, Vol. 36, pp. 385-390, 2009.

[5] Yin X. and Bau H. H., "Axial Conduction Effect Performance of Micro Heat Exchangers", ASME Winter Annual Meeting, New Orleans, Louisiana, USA, November 28-December 3, 1992.

[6] Stief T., Langer O. U. and Schubert K., "Numerical Investigation of Optimal Heat Conductivity in Micro Heat Exchangers", Chem Engineering Technology, Vol. 22, pp. 297-303, 1999.

[7] Hussien Al-bakhit and Ahmad Fakheri, "Numerical Simulation of Heat Transfer in Simultaneously Developing Flows in Parallel Rectangular Ducts", Applied Thermal Engineering, Vol. 26, pp. 596-603, (2006).

[8] Mushtaq I. Hasan, "Numerical Simulation of Counter Flow Microchannel Heat Exchanger with Different Channel Geometries and Working Fluid", PhD Thesis, Mechanical Engineering Department, Collage of Engineering, Basrah University, 2009.

[9] **Hyder M. Hasan, "** Numerical Simulation of Parallel Flow Microchannel Heat Exchanger with Isosceles Right Triangular Geometry", MSc Thesis, Engineering Collage, University of Basrah, 2009.

[10] Sean Ashman and Satish G. Kandlikar, "A review of Manufacturing Processes for Microchannel Heat Exchanger Fabrication", Proceedings of ICNMM2006, Fourth International Conference on Nanochannels, Microchannels and Minichannels, Limerick, Ireland, June 19-21 (2006).

[11] H. K. Versteeg and W. Malalasekera, "An introduction to Computational Fluid Dynamics-The Finite-Volume Method", Longman, (1995).

[12] Amit S. Kulkarni, "Effects of Surface Roughness in Microchannel Flows", MSc Thesis, University of Florida, (2004).